

# Application of an ePix100 detector for coherent scattering using a hard X-ray free-electron laser

Marcin Sikorski,\* ‡ Yiping Feng, Sanghoon Song, Diling Zhu, Gabriella Carini, Sven Herrmann, Kurtis Nishimura, Philip Hart and Aymeric Robert

Linac Coherent Light Source, SLAC National Accelerator Laboratory, 2575 Sand Hill Road, Menlo Park, CA 94025, USA.

\*Correspondence e-mail: marcin.sikorski@xfel.eu

Received 25 January 2016

Accepted 5 July 2016

Edited by M. Yabashi, RIKEN SPring-8 Center, Japan

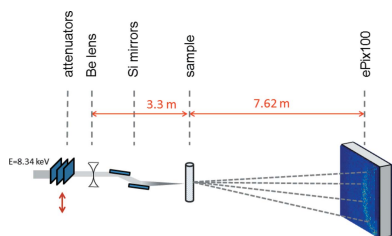
‡ Current address: European XFEL GmbH, Holzkoppel 4, 22869 Schenefeld, Germany.

**Keywords:** X-rays; free-electron laser (FEL); detector; droplet algorithm; coherent scattering.

A prototype ePix100 detector was used in small-angle scattering geometry to capture speckle patterns from a static sample using the Linac Coherent Light Source (LCLS) hard X-ray free-electron laser at 8.34 keV. The average number of detected photons per pixel per pulse was varied over three orders of magnitude from about 23 down to 0.01 to test the detector performance. At high average photon count rates, the speckle contrast was evaluated by analyzing the probability distribution of the pixel counts at a constant scattering vector for single frames. For very low average photon counts of less than 0.2 per pixel, the ‘droplet algorithm’ was first applied to the patterns for correcting the effect of charge sharing, and then the pixel count statistics of multiple frames were analyzed collectively to extract the speckle contrast. Results obtained using both methods agree within the uncertainty intervals, providing strong experimental evidence for the validity of the statistical analysis. More importantly it confirms the suitability of the ePix100 detector for X-ray coherent scattering experiments, especially at very low count rates with performances surpassing those of previously available LCLS detectors.

## 1. Introduction

In the past decade, several short-wavelength free-electron laser (FEL) sources have been built and are in user operation, most notably the Free-electron LASer at Hamburg (FLASH) (Ackermann *et al.*, 2007), the Linac Coherent Light Source (LCLS) (Emma *et al.*, 2010), the SPring-8 Angstrom Compact free-electron LASer (SACLA) (Ishikawa *et al.*, 2012) and the FERMI@Elettra free-electron laser (Allaria *et al.*, 2012). Many more facilities are being constructed, including the European XFEL in Germany, the SwissFEL in Switzerland and the PAL-XFEL in Korea. The extraordinary properties of the FEL radiation, including the unprecedented peak brightness, the nearly full transverse coherence and the ultrashort pulse duration, coupled with a growing list of new capabilities, such as transform-limited pulses by self-seeding (Ratner *et al.*, 2015; Amann *et al.*, 2012) or multiple colors (Lutman *et al.*, 2013; Marinelli *et al.*, 2015; Hara *et al.*, 2013), have been used and will continue to be explored to push the boundaries of a broad range of scientific endeavors ranging from structural biology and ultrafast chemistry to nonlinear light–matter interactions and warm dense matter (Bostedt *et al.*, 2016). In keeping pace with the recent advancements in source capabilities, the development in beam diagnostics, optics, sample delivery, detectors and data acquisition/analysis must also be concurrently pursued in order to fully realise the scientific potential of FELs.



Significant progresses in making detectors suitable for using with X-ray FEL beams have been much less forthcoming due to many challenging requirements for a variety of experimental measurements. Up until now, only a very few detectors have been available and utilized successfully at LCLS (Blaj *et al.*, 2015), which started operation in 2009 and delivers either soft (280 eV to 2 keV) or hard X-ray (4 keV to 12.8 keV) radiation to seven experimental instruments supporting diverse frontier research activities (White *et al.*, 2015). The charge-coupled device (CCD) detectors provide low noise along with good energy resolution over a wide range of X-ray energies. They offer single photon detection suitable for sub-pixel resolution, features desired by numerous techniques utilized at FELs. Unfortunately, only very few of the CCD detectors can support readout speeds matching the LCLS repetition rate. The pnCCD camera (Strüder *et al.*, 2010) is often the detector of choice because of its low noise and high quantum efficiency. Another example of the CCD camera used at LCLS is the fCCD detector (Doering *et al.*, 2011; Strüder *et al.*, 2010) with small pixel size of  $30\ \mu\text{m} \times 30\ \mu\text{m}$ . A large fraction of experiments performed in the hard X-ray range uses the Cornell–SLAC Pixel Array Detector (CSPAD) (Hart *et al.*, 2012a), the first generation of an integrating detector with a pixel size of  $110\ \mu\text{m} \times 110\ \mu\text{m}$  developed specifically for LCLS. The CSPAD camera has performed well and consistently and is the main hard X-ray detector at LCLS. CSPAD cameras consisting of 2 to 64 individual modular units (Hart *et al.*, 2012b; Herrmann *et al.*, 2013) are routinely used at the four LCLS hard X-ray instruments. For the newest version of the CSPAD, the signal in the dark images was measured to be approximately  $\sigma_{\text{Gauss}} = 0.125 \pm 0.001$  photons at 8.34 keV, which could limit the detection of very weak signals or signal fluctuations. A number of experimental techniques, especially X-ray coherent scattering, could benefit greatly from a detector with a noise level significantly lower than that of the CSPAD.

A new detector optimized for single-photon detection in the hard X-ray photon energy range, ePix100, has been in development at SLAC National Accelerator Laboratory. It implements several key features, identified from the user experiences gained during the first years of the LCLS operation. In addition to matching the readout speed to the LCLS repetition rate, the main requirements for the new detector are:

**Low noise.** Improvement in single-photon detection over the current CSPAD performance is highly desired. In spite of the fact that FELs deliver ultra-intense pulses, many experimental techniques rely on the acquisition of weak signals or, as is the case for the pump–probe type of experiments, are sensitive to small fluctuations in the incident beam intensity. Among the factors limiting the output signal are the small scattering cross section of the sample and low efficiency of the overall detection scheme. Frequently, only a small fraction of the available incident flux is utilized during measurements to reduce the risk of radiation damage to the sample. This is especially important for techniques that require the same part of the sample to be illuminated by multiple pulses, *e.g.* X-ray

photon correlation spectroscopy (XPCS) (Carnis *et al.*, 2014) or time-resolved coherent X-ray diffraction imaging (Clark *et al.*, 2013).

**Small pixel size.** For scattering or diffraction experiments, the pixel size determines the resolution in the real or reciprocal space, respectively, while in the case of energy-dispersive measurements such as X-ray emission spectroscopy it sets the energy resolution. To achieve a given resolution, a trade-off must be made between the pixel size and the maximum attainable sample-to-detector distance, which is often limited by the footprint of the experimental hutch. For X-ray coherent scattering techniques such as XPCS, a smaller pixel size is again advantageous since a larger area for sample illumination can be used for minimizing radiation damage.

**Compact and modular design.** Measurements conducted nowadays with hard X-rays became very elaborate and require complex and compact experimental arrangements. As a consequence, detectors are often also expected to be more compact and to require more flexible support infrastructure such as chillers or vacuum pumps. Many experiments share common needs in term of detector response to incident radiation but it is challenging to define the shape and size of the detector that suits all scientific cases. One of the desired characteristics of a FEL detector is a modular design allowing fabrication of a custom-shape detector from simple building blocks.

The new detector, ePix100, was developed at LCLS to satisfy the requirements listed above. A prototype unit consisting of a small ePix100 module has been assembled and tested recently. Its performances, particularly in terms of noise, were evaluated in an X-ray coherent scattering experiment. This class of measurements is particularly well suited for testing this detector requirement. Here we describe technical challenges in producing the optimal speckle pattern, with the emphasis on matching the ePix100 small pixel size to the experimental configuration. Speckle patterns from a static sample were acquired over a broad range of incident flux to assess detector performances over its entire dynamic range. Statistical analysis of the acquired patterns was performed to extract the coherence properties of the incident beam. Obtained results are consistent between applied methods, validating the data analysis and more importantly establishing the ePix100 detector suitability for X-ray FEL applications, especially for those dealing with signal count rates below 1 photon per pixel per pulse.

## 2. Experimental setup and methods

Our measurements were carried out at the X-ray correlation spectroscopy (XCS) (Alonso-Mori *et al.*, 2015) instrument, one of the hard X-ray instruments of the LCLS. The X-ray FEL was operating in the self-amplified spontaneous emission (SASE) (Bonifacio *et al.*, 1984) mode with an optimal compression for producing maximum pulse energies. The photon energy was set to 8.34 keV, and the FEL pulses were nominally 50 fs long with an average intensity of 2 mJ. The layout of the experimental setup is shown schematically in

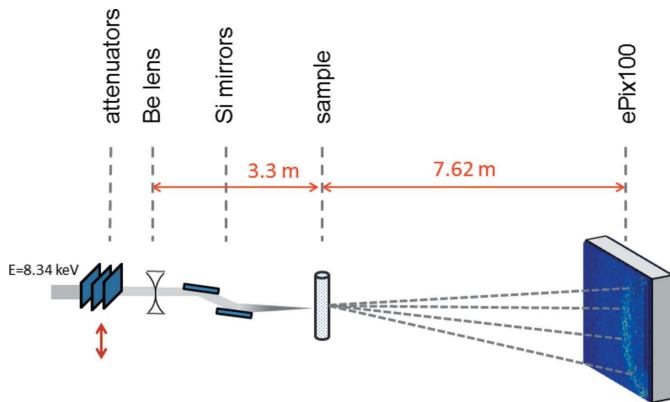


**Figure 1**  
Schematic layout of the experimental setup, including attenuators, beryllium lens for focusing, silicon flat mirrors for filtering high-order harmonics, silica nanosphere sample in a thin capillary, and ePix100 detector.

Fig. 1. Solid attenuators composed of single-crystal silicon thin plates were used to vary the incident intensity on the sample by over three orders of magnitude. A stack of beryllium compound refractive lenses with an effective focal length  $f = 3.3$  m were used to adjust the beam size at the sample plane. The high harmonic content of the FEL radiation was suppressed with the help of a pair of silicon mirrors.

The static sample consists of dry silica spheres. The dry powder was loaded into a quartz capillary of diameter 1 mm, and placed at the center of the diffractometer (not shown). The large nominal diameter of the particles (150 nm) ensures strong scattering in the forward direction. The ePix100 detector was mounted 7.62 m downstream of the sample. The average number of photons per pixel per pulse,  $k_{\text{avg}}$ , in the recorded speckle images was varied systematically from approximately  $k_{\text{avg}} > 20$  down to  $k_{\text{avg}} < 0.01$ . For a given incident flux at the sample, data sets of up to 10000 single-pulse images were collected. A series of 5000 dark images were recorded every few minutes to keep track of the background noise level in the camera as a function of time.

### 2.1. Characteristics of the ePix100 detector

A new generation of cameras for LCLS, the ePix detectors (Blaj *et al.*, 2015), was recently developed at SLAC to enhance and augment the LCLS’s detector capabilities beyond those of the CSPAD. Specifications and characteristics of the ePix ASICs have been described previously (Dragone *et al.*, 2014). The ePix cameras come in two flavors. The ePix10K offers a high dynamic range of  $10^3$  photons at 8 keV and has  $100 \mu\text{m} \times 100 \mu\text{m}$  pixels, while the ePix100 has smaller  $50 \mu\text{m} \times 50 \mu\text{m}$  pixels and is optimized for low-noise operation with the maximum signal limited to 100 photons at 8 keV. Both use either a 300  $\mu\text{m}$  or 500  $\mu\text{m}$ -thick n-type high-resistivity ( $>5 \text{ k}\Omega \text{ cm}^{-1}$ ) silicon sensor to maximize the quantum efficiency at hard X-ray energies. For the measurements reported here,  $384 \times 352$  pixels module with the 300  $\mu\text{m}$  sensor biased with 200 V was used.

### 2.2. Introduction to speckle patterns

One of the most important features that distinguishes X-ray FELs from the previous generations of sources including those at the state-of-the-art storage-ring-based facilities is the nearly full transverse coherence of the beam. X-ray scattering of a coherent beam from a disordered network of objects forms an interference pattern, also known as speckles (Goodman, 2006). The spatial intensity distribution of the X-ray speckles is determined by the instantaneous configuration of the scatterers in the illuminated volume at a given point in time. The relative motions of the scatterers would then give rise to the temporal evolution of the corresponding X-ray speckle pattern, providing a means for studying the sample dynamics, in much the same way as in dynamic light scattering (Berne & Pecora, 2000). The technique of X-ray photon correlation spectroscopy (Grübell *et al.*, 2008) was developed only after sufficient coherent flux could be obtained at the third-generation synchrotron sources with insertion devices and has been applied successfully to a large number of dynamic disordered systems (Sutton, 2008).

Quantitative analysis of a speckle pattern is typically performed by evaluating its intensity fluctuations, which depends on the degrees of coherence of the incident radiation, both spatial and temporal, and is described by the contrast parameter  $\beta$ . The contrast is inversely proportional to the effective number of coherent modes in the incident radiation seen by the sample,  $\beta = 1/\sqrt{M_{\text{eff}}}$ . A contrast  $\beta = 1$  is expected for a pattern formed by a fully coherent field, whereas  $\beta = 0$  in the case of a fully incoherent light. It should be stressed that  $M_{\text{eff}}$  estimated from the recorded speckle pattern is, in general, greater than the number of modes in the FEL radiation itself. The measured coherence of the beam can be reduced by the imperfections of the beamline optics and the experimental geometry, thus increasing  $M_{\text{eff}}$ . In addition, the relative area of a single detector element in relation to the speckle size can alter the intensity fluctuation measurement, potentially modifying  $M_{\text{eff}}$  as well. The detector contribution to  $M_{\text{eff}}$  can be typically minimized by ensuring that the average speckle size  $S$  is greater than or equal to the detector pixel size. This can be achieved by trading off the photon wavelength  $\lambda$ , beam size at the sample location  $d$ , or sample-to-detector distance  $L$  according to the following relation:

$$S = \alpha \frac{\lambda L}{d}, \quad (1)$$

where the prefactor  $\alpha$  is used to account for beam and detector properties.

One way to accommodate the relatively large pixel sizes of currently available detectors ( $110 \mu\text{m} \times 110 \mu\text{m}$  for the CSPAD and  $75 \mu\text{m} \times 75 \mu\text{m}$  for the pnCCD) is to focus the beam at the sample location to generate larger speckles. In practice,  $d$  is often limited by the focusing optics but more importantly the single-shot radiation damage threshold of the sample. An alternative solution is to increase the sample-to-detector distance. However, even a focus of several micrometers translates into  $L$  being of the order of several meters. For example, in the case of an 8 keV beam focused down to

$d = 5 \mu\text{m}$ , the CSPAD has to be positioned at more than 7 m downstream from the sample to match the average speckle size to its pixel size. Detectors with smaller pixel sizes would allow for reduction in the overall dimensions of the experimental apparatus or would help mitigate the radiation damage concern (Sikorski *et al.*, 2015).

### 3. Data analysis and results

#### 3.1. Data processing

The raw images were first subtracted by the average dark image. Common-mode (Blaj *et al.*, 2015), background and gain corrections were applied taking into account the different outputs and subsection organization of the chip. Bad pixels were masked out and discarded from further analysis. An example of a processed single-pulse image acquired near the upper limit of the dynamic range of the ePix100 is shown in Fig. 2(a). The borders between the segments of the image are marked with dashed lines. Besides parts of the sensor close to its edges, most of the segment labeled as ‘#1’ had a high concentration of damaged and noisy pixels. On average, 0.4% of pixels were identified as damaged or noisy for the remaining part of the sensor.

The high degree of coherence of the incident FEL beam is clearly reflected by the grainy texture, or speckle nature, of the recorded image. As expected for an ensemble of concentrated spherical nano-particles, the speckles form concentric rings. The average speckle size,  $S \simeq 70 \mu\text{m}$ , was estimated from the spatial autocorrelation function of the intensity of the individual speckle patterns. The pixel coordinates were mapped onto the momentum transfer  $q$  based on the X-ray wavelength and the experimental geometry, and pixels of similar  $q$  were binned into narrow regions, referred to as partitions. The small-angle X-ray scattering curve, the average number of photons in each partition as a function of  $q$ , is plotted in Fig. 2(b). The rings captured in the speckle patterns are represented by the two broad peaks. The more intense one, at  $q = 0.005 \text{ \AA}^{-1}$ , *i.e.* the structure factor peak, corresponds to the characteristic distance between neighboring silica spheres in the sample, while the second one, at  $q = 0.0085 \text{ \AA}^{-1}$ , comes from the average form factor of the silica particles themselves. The SAXS intensity [circles in Fig. 2(b)] calculated from the images acquired using ePix100 matches extremely well the data collected with a CSPAD for the same sample [triangles in Fig. 2(b)].

The histogram of the analog-to-digital units (ADU) of the pixels in segment ‘#3’ is shown in Fig. 2(c), where the one- and two-photon peaks are approximately located at 127 ADU and 254 ADU, respectively. The position of the one-photon peak changes by less than 2 ADU as shown in the inset of Fig. 2(c). The noise peak centered at 0 ADU was obtained from the dark images and is plotted with a dashed line. A uniform noise with a standard deviation  $\sigma_{\text{Gauss}} = 4.5 \pm 0.01 \text{ ADU}$  was measured across the entire sensor. Based on  $\sigma_{\text{Gauss}}$ , the noise cutoff was set to 10 ADU ( $>2\sigma_{\text{Gauss}}$ ). Pixels

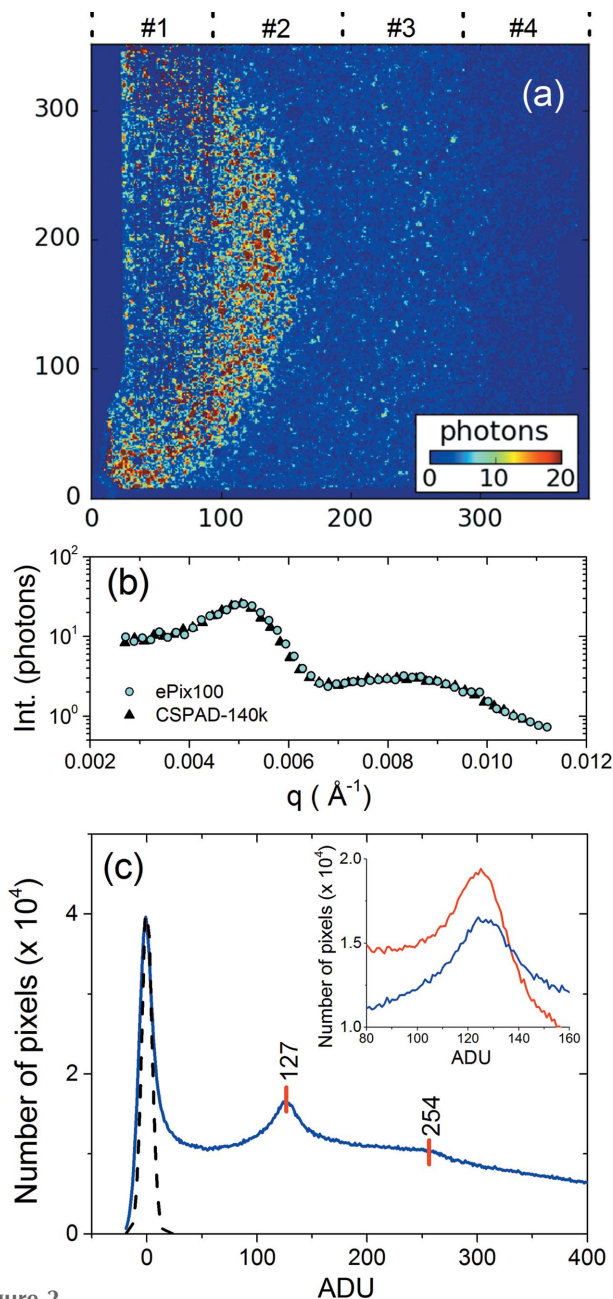


**Figure 2**  
 (a) Single-pulse speckle pattern from a dry powder of silica nanospheres collected with the ePix100 detector. The borders between 96 pixels wide segments of the image (labeled ‘#1...#4’) are marked with vertical dashed lines. Masked pixels were set to 0. (b) Small-angle X-ray scattering curve calculated from a set of 10000 images acquired using the ePix100 (circles) and CSPAD-140k (triangles). (c) Histogram of the analog-to-digital units per pixel calculated for segment #3. The one- and two-photon peaks are located at 127 ADU and 254 ADU, respectively. The noise peak (dashed line) was obtained from dark images and scaled to the data. Inset: the one-photon peak measured for segments ‘#3’ (blue) and ‘#4’ (red).

lower than 10 ADU were assumed not to register any signal and were set to 0 for subsequent analysis.

#### 3.2. Computation of speckle contrast

In the count rate regime supported by the ePix100, the statistics in the recorded images are a convolution of the

intrinsic statistics of the speckle pattern and the photon-counting statistics. The probability  $P(k)$  of a pixel detecting exactly  $k$  photons for a fully developed speckle can be described by a negative binomial probability distribution function (Goodman, 2006):

$$P(k) = \frac{\Gamma(k + M_{\text{eff}})}{\Gamma(k + 1)\Gamma(M_{\text{eff}})} \left( \frac{k_{\text{avg}}}{k_{\text{avg}} + M_{\text{eff}}} \right)^k \left( \frac{M_{\text{eff}}}{k_{\text{avg}} + M_{\text{eff}}} \right)^{M_{\text{eff}}}, \quad (2)$$

where  $k_{\text{avg}}$  is the average number of photons in a given pixel and  $M_{\text{eff}}$  is the effective number of the transverse modes in the incident beam if the effect of the temporal coherence is negligible. The extent of the intensity fluctuations in the recorded speckle, in the framework of this distribution, is a function of  $k_{\text{avg}}$  and  $M_{\text{eff}}$ :

$$C = \frac{\sigma_k}{k_{\text{avg}}} = \left( \frac{1}{M_{\text{eff}}} + \frac{1}{k_{\text{avg}}} \right)^{1/2}, \quad (3)$$

where  $\sigma_k$  denotes the standard deviation of the count rate  $k$ .

**3.2.1. High  $k_{\text{avg}}$  data.** First, we analyzed speckle patterns acquired at the upper limit of the incident intensity with individual pixels exposed up to the 100 photons limit. In this regime,  $k_{\text{avg}}$  ranged from around 20 photons per pixel for the partition matching the structure factor ring to below 2 photons for the largest accessible  $q$ , and the analysis was performed on individual images. For each partition,  $P(k)$  was fitted to a negative binomial distribution given by equation (2), with  $k_{\text{avg}}$  and  $M_{\text{eff}}$  both being the fitting parameters. Analysis was restricted to partitions with  $k_{\text{avg}} > 5$  photons per pixel. In the case of partitions having lower  $k_{\text{avg}}$ , the maximum of  $P(k)$  was below 1 photon and the fitting routine converged artificially to the  $M_{\text{eff}} = 1$  solution, rendering the analysis challenging and requiring an alternative analytical approach to be discussed in the following section on this report. A typical  $P(k)$  along with the fit is shown in Fig. 3(a) for a single frame at  $q = 0.005 \text{ \AA}^{-1}$ , yielding  $k_{\text{avg}} = 24.0 \pm 5.0$  photons and  $M_{\text{eff}} = 2.35 \pm 0.20$ .

The fitting parameters and the results of the analysis for other  $q$  values are summarized in Figs. 3(b)–3(d). Each data point is an average of the fitting parameter over 1100 individual patterns of similar exposure levels. The average number of photons per pixel  $k_{\text{avg}}$  obtained from the fit to  $P(k)$  agrees very well with the directly measured average scattering intensity (dashed curve in Fig. 3b), reaffirming the statistical model in equation (2). The effective number of transverse coherent modes, which in principle is independent of the scattered intensity and the momentum transfer  $q$ , is observed to be constant as expected with an average value of  $M_{\text{eff}} = 2.25$  within the experimental uncertainties as indicated by the error bars (Fig. 3c). The larger error bars for the smaller  $q$  data are due to the poorer statistics associated with the smaller number of total pixels in a particular partition. The obtained value of  $M_{\text{eff}}$  corresponds to the speckle pattern contrast  $\beta = 0.67$ . The value of the parameter  $C$  [equation (3)] is shown in Fig. 3(d).

**3.2.2. Low  $k_{\text{avg}}$  data.** In the other limit, when  $k_{\text{avg}}$  is very low ( $< 0.2$  photons per pixel per pulse),  $\sigma_k$  of the intensity in the

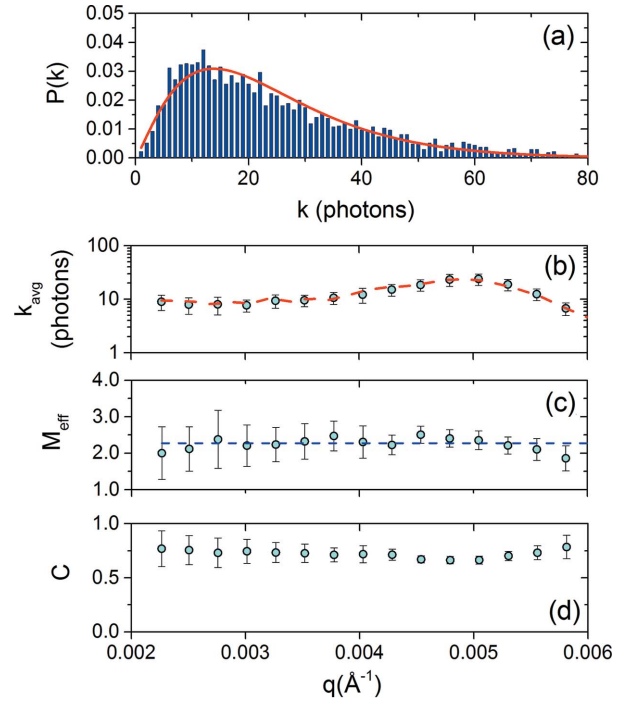


**Figure 3**

(a) Example of the intensity probability distribution  $P(k)$  calculated for  $q = 0.005 \text{ \AA}^{-1}$  from a single-pulse speckle pattern. The solid line represents the best fit to a negative binomial distribution [equation (2)] for  $k_{\text{avg}} = 24.0 \pm 0.2$  photons and  $M_{\text{eff}} = 2.35 \pm 0.20$ . (b) The average number of photons  $k_{\text{avg}}$ , (c) the effective number of transverse modes  $M_{\text{eff}}$  at different wavevector transfers  $q$  and (d) the normalized standard deviation  $C$  calculated from equation (3). The red dashed line in (b) is a low  $q$  part of the small-angle X-ray scattering curve from Fig. 2(b). The dashed line in (c) marks  $M_{\text{eff}} = 2.35$ . Data points in (b), (c) and (d) are averages of the fitting parameters over 1100 individual patterns of similar exposure levels.

speckle pattern becomes dominated by the photon-counting statistics [the contribution given by  $1/k_{\text{avg}}$  in equation (3)]. The viability of the  $k_{\text{avg}}$  data analysis is determined by the detector's ability to resolve the signal at a single-photon level above the background. A typical speckle pattern with  $k_{\text{avg}}$  below 0.1 photon per pixel is shown in Fig. 4(a). In this low illumination regime, the noise performance of the ePix100 could be thoroughly tested. The association of a discrete photon count number with a particular pixel requires the use of a so-called droplet algorithm (Livet *et al.*, 2000; Hruszkewycz *et al.*, 2012), which is a well established image-processing tool routinely used to correct for charge sharing among pixels for pixelated detectors.

The droplet algorithm has been described in detail previously (Hruszkewycz *et al.*, 2012). Here, we only highlight the two main steps. First, a cluster of pixels (droplets) sharing photons are identified. Then, the positions of the individual photons are calculated based on the ADU distribution within the droplets. The performance of the droplet analysis is strongly coupled to the performance of the detector, particularly its intrinsic noise level. With decreasing noise a smaller fraction of a photon can be resolved in an individual pixel. As a result, a larger number of photons per droplet can be correctly identified. The algorithm works for a limited  $k_{\text{avg}}$

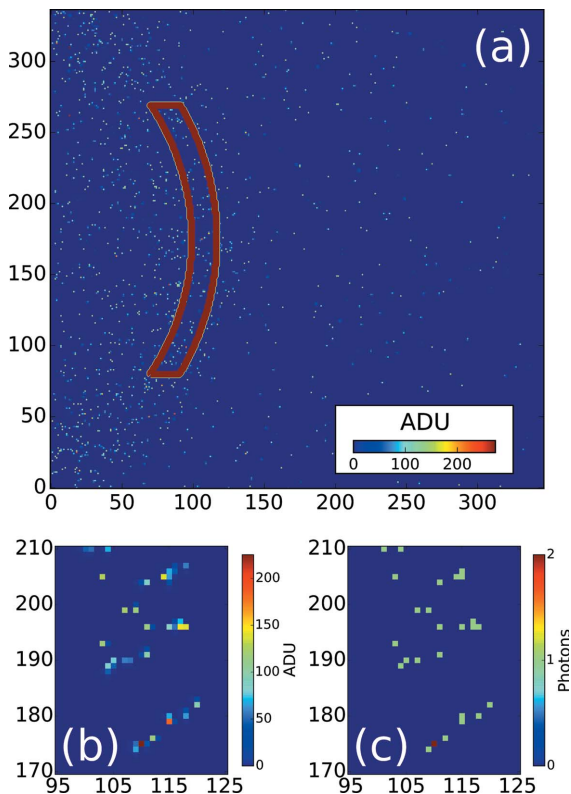


**Figure 4** (a) Single-pulse speckle pattern collected using ePix100 under the low illumination conditions. The red lines mark the region of interest (ROI) used for the droplet analysis (see text for details). The average number of photons per pixel inside the ROI is  $k_{\text{avg}} = 0.036$ . Plots (b) and (c) show part of the ROI before and after the droplet analysis, respectively.

range. Above approximately 0.2 photons per pixel per pulse, droplets start to connect and merge together, causing the first step of the droplet analysis to fail. The lowest  $k_{\text{avg}}$  for which  $M_{\text{eff}}$  can be estimated is set by the number of pixels  $n_{\text{pix}}$  used for the analysis. In principle, at least one pixel with more than one photon is needed to calculate  $M_{\text{eff}}$ . The expected number of pixels with two photons becomes less than one for  $k_{\text{avg}} < k_{\text{min}} \simeq (2/n_{\text{pix}})^{1/2}$  in the large  $M_{\text{eff}}$  limit (Hruszkewycz *et al.*, 2012). In the case of the ePix100 data, the region of interest [indicated by the solid line in Fig. 4(a)] is a single partition consisting of  $n_{\text{pix}} = 5200$  ( $k_{\text{min}} = 0.02$ ) centered at the structure factor ring ( $q = 0.005 \text{ \AA}^{-1}$ ). To minimize the impact of masked pixels on the outcome of the droplet analysis, parts of the structure factor ring belonging to segment ‘#1’ were excluded from the analysis. Owing to the low noise of ePix100, droplets with up to 10 photons could be resolved in the collected patterns. In the histogram of ADU per droplet depicted in Fig. 5, the single and multiple photons are represented by ten peaks evenly spaced by 127 ADU. The thresholds used to convert the total number of ADU in a droplet to an integer number of photons are marked by the dashed lines in Fig. 5. Droplets containing less than 63 ADU were considered as noise and thus discarded from further analysis. Next, photons were distributed among the pixels in the droplets (Hruszkewycz *et al.*, 2012). A typical outcome of the analysis is

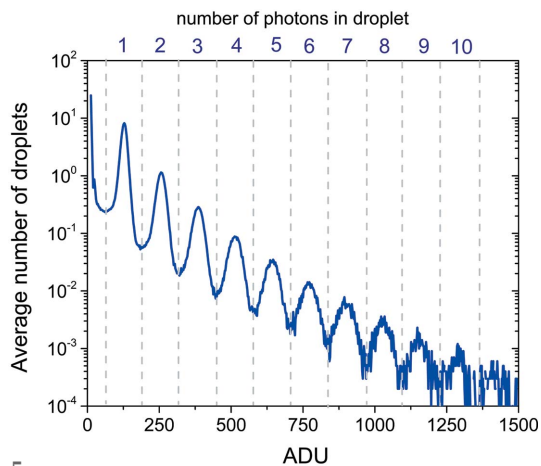


**Figure 5** Histogram of the analog-to-digital units per droplet averaged over 10000 images. Dashed lines mark thresholds used to assign integer number of photons per droplet.

presented in Figs. 4(b) and 4(c) showing several droplets from the pattern in Fig. 4(a) before and after the application of the droplet algorithm.

The probability of individual pixels detecting  $k = 1, 2, 3, 4$  photons as a function of  $k_{\text{avg}}$  is plotted in Fig. 6. It should be noted that each data point in Fig. 6 is an average over many hundreds to thousands of processed images of the same  $k_{\text{avg}}$ . The probability  $P(k)$  was modeled using the negative binomial distribution [equation (2)]. The measured  $P(k)$  matches best with the predicted probability for  $M_{\text{eff}} = 2.5 \pm 0.2$  as shown by the solid lines in Fig. 6. This value is in very good agreement with  $M_{\text{eff}} = 2.25 \pm 0.15$  obtained from the single-frame analysis for  $k_{\text{avg}} > 20$ , lending further credence to the statistical modeling for both low- and high-illumination conditions. The predicted probabilities for the complete coherent case  $M_{\text{eff}} = 1$

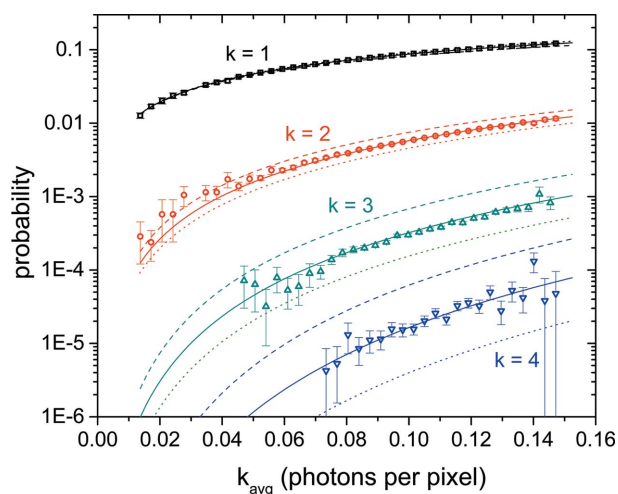


**Figure 6** Probability  $P(k)$  of detecting  $k = 1, 2, 3, 4$  photons as a function of the averaged number of photons per pixel  $k_{\text{avg}}$  in the speckle pattern. Probabilities were evaluated based on series of 22443 single-pulse images recorded for  $0.015 < k_{\text{avg}} < 0.16$  photons per pixel. Solid lines represent the best fit using a negative binomial distribution [equation (2)] for  $M_{\text{eff}} = 2.5 \pm 0.2$ . Predictions for  $M_{\text{eff}} = 1$  and  $M_{\text{eff}} = 100$  are shown with dotted and dashed lines, respectively.

and a highly incoherent case of  $M_{\text{eff}} = 100$  are also shown in Fig. 6 for comparison. The contrast of the speckle pattern was again calculated to be  $\beta = 1/\sqrt{M_{\text{eff}}} = 0.63 \pm 0.02$ .

In addition to the enhancement of the collected images for improved speckle analysis, the droplet analysis provides a way to estimate the dimensions of a charge cloud created by a single photon. As described by Abboud *et al.* (2013), the size distribution of the one-photon droplets is determined by the ratio of the charge cloud to the pixel size. We observed that approximately 48% of all one-photon droplets were constrained to a single pixel, while 40%, 9% and 3% of droplets extended over two, three and four pixels. This distribution corresponds to the electron charge cloud radius of approximately  $R = 17.0 \mu\text{m}$ .

#### 4. Discussion and conclusions

The presented X-ray coherent scattering measurements have yielded several important findings on the ePix100 performance. First and foremost, it offers significantly lower noise compared with the CSPAD detector. In Fig. 7, the normalized histograms of the dark images collected using the ePix100 detector and the CSPAD are shown. The ADU units were converted to photons in Fig. 7 based on their respective one-photon peak positions. The standard deviation of the intrinsic noise for the ePix100,  $\sigma_{\text{Gauss}} = 0.036 \pm 0.0004$  photons, is about a factor of three lower than that of the CSPAD at  $\sigma_{\text{Gauss}} = 0.125 \pm 0.001$  photons. As a consequence, the ePix100 enables the identification of a three times smaller fraction of a photon and the ability to resolve up to 10 photons per pixel as depicted in Fig. 5. A number of techniques utilized at the LCLS such as coherent diffraction imaging or photon correlation spectroscopy could potentially gain significant improvement in their single-photon detection capabilities in the hard X-ray photon energy range. This is very important for measuring scattered intensities at large momentum transfers to achieve higher structural resolution.

The demonstrated capability of the ePix100 detectors to resolve well the contrast of a speckle pattern under low illu-

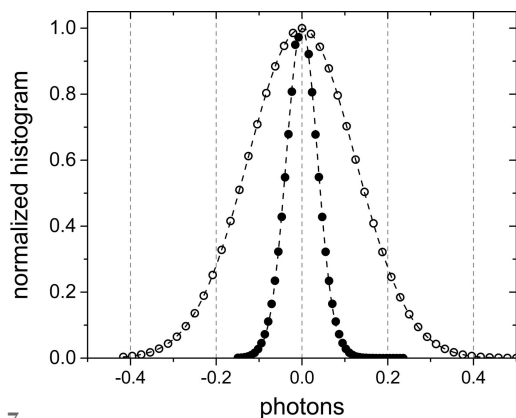


**Figure 7** Normalized histograms of photons per pixel for ePix100 (filled symbols) and CSPAD version 1.7 (open symbols) calculated from dark images. Dashed lines represent the best fit using a Gaussian line profile with  $\sigma_{\text{Gauss}} = 0.036 \pm 0.0004$  photons and  $\sigma_{\text{Gauss}} = 0.125 \pm 0.001$  photons for ePix100 and CSPAD, respectively.

mination conditions is especially important in light of the recent progress in the LCLS double pulse mode of operation (Marinelli *et al.*, 2015). Routine generation of two pulses with tunable delay on the order of picoseconds or nanoseconds will provide a novel tool to study fast dynamics in condensed matter, which is complementary to the X-ray optics based techniques (Gutt *et al.*, 2009; Sorgenfrei *et al.*, 2010). In the double pulse scheme, the speckle patterns generated by two pulses are recorded in a single frame as a sum. The characteristic time-scale of the dynamics of the system under study is obtained from an increase of  $M_{\text{eff}}$  (a reduction in contrast  $\beta$ ) in the summed speckle pattern as a function of the delay time between the pulses. One of the critical components required to realise such an experiment is a detector optimized for  $M_{\text{eff}}$  measurements. As emphasized in the *Introduction*, for various reasons the acquired speckle patterns are expected to consist of only a few photons per image. Our data clearly showed that the ePix100 is well suited for contrast measurements at low average count rate. Although it is sufficient to use the two-photon events to estimate  $M_{\text{eff}}$ , the precision of the measurement improves dramatically if events of multiple photons of more than two are also present. This is illustrated in Fig. 6 showing  $M_{\text{eff}} = 1.0$  and  $M_{\text{eff}} = 100$  for  $k = 1, 2, 3, 4$ . To improve the efficiency of detecting multi-photon events and thus to achieve higher precision on single-pulse contrast measurements, larger area ePix100 detectors would be required. The small footprint of the ePix100 along with its modular design makes it easy to utilize multiple detectors even for crowded experimental setups.

The readout speed is another important parameter to consider when selecting a detector. Often, to obtain statistically relevant information of the underlying phenomena and to account for pulse-to-pulse fluctuations of the FEL beam properties, the measurement needs to be repeated multiple times. To maintain a high efficiency of data acquisition, it is crucial for the detector to operate at high speed. The PI-LCX:1300 from Princeton Instruments is an example of a detector which was successfully used for proof-of-principle experiments such as contrast measurements in the high (Gutt *et al.*, 2012) and low (Hruszkewycz *et al.*, 2012) count rate regimes. However, its readout time of several seconds makes it unsuitable for many types of measurements at LCLS. In contrast, the speed of the new ePix detectors can match the full repetition rate of the LCLS for optimizing data acquisition efficiency.

In conclusion, the ePix100 detector was tested based on contrast analysis of a static X-ray speckle pattern. The low-noise performance was tested at low average pixel counts for single- and few-photon events. Two statistical methods were used: for high average photon counts whereby the speckle contrast was evaluated by analyzing the probability distribution of the pixel counts at a constant scattering vector in a single frame; and, for very low average photon counts, the droplet algorithm was applied prior to the analysis to correct for charge sharing. The results of the two methods agree within the accuracy of the applied analysis. The significantly improved noise performance of the ePix100 detector will

likely make it the detector of choice for various types of measurements such as X-ray coherence based techniques or spectroscopy.

### Acknowledgements

Use of the Linac Coherent Light Source, SLAC National Accelerator Laboratory, is supported by the US Department of Energy, Office of Science, Office of Basic Energy Sciences under Contract No. DE-AC02-76SF00515.

### References

Abboud, A., Send, S., Pashniak, N., Leitenberger, W., Ihle, S., Huth, M., Hartmann, R., Strüder, L. & Pietsch, U. (2013). *J. Instrum.* **8**, P05005.

Ackermann, W., Asova, G., Ayvazyan, V., *et al.* (2007). *Nat. Photon.* **1**, 336–342.

Allaria, E., Appio, R., Badano, L., Barletta, W., Bassanese, S., Biedron, S., Borga, A., Busetto, E., Castronovo, D., Cinquegrana, P., Cleva, S., Cocco, D., Cornacchia, M., Craievich, P., Cudin, I., D’Auria, G., Dal Forno, M., Danailov, M., De Monte, R., De Ninno, G., Delgiusto, P., Demidovich, A., Di Mitri, S., Diviacco, B., Fabris, A., Fabris, R., Fawley, W., Ferianis, M., Ferrari, E., Ferry, S., Froehlich, L., Furlan, P., Gaio, G., Gelmetti, F., Giannessi, L., Giannini, M., Gobessi, R., Ivanov, R., Karantzoulis, E., Lonza, M., Lutman, A., Mahieu, B., Milloch, M., Milton, S., Musardo, M., Nikolov, I., Noe, S., Parmigiani, F., Penco, G., Petronio, M., Pivetta, L., Predonzani, M., Rossi, F., Rumiz, L., Salom, A., Scafuri, C., Serpico, C., Sigalotti, P., Spampinati, S., Spezzani, C., Svandrlik, M., Svetina, C., Tazzari, S., Trovo, M., Umer, R., Vascotto, A., Veronese, M., Visintini, R., Zaccaria, M., Zangrando, D. & Zangrando, M. (2012). *Nat. Photon.* **6**, 699–704.

Alonso-Mori, R., Caronna, C., Chollet, M., Curtis, R., Damiani, D. S., Defever, J., Feng, Y., Flath, D. L., Glowia, J. M., Lee, S., Lemke, H. T., Nelson, S., Bong, E., Sikorski, M., Song, S., Srinivasan, V., Stefanescu, D., Zhu, D. & Robert, A. (2015). *J. Synchrotron Rad.* **22**, 508–513.

Amann, J., Berg, W., Blank, V., Decker, F.-J., Ding, Y., Emma, P., Feng, Y., Frisch, J., Fritz, D., Hastings, J., Huang, Z., Krzywinski, J., Lindberg, R., Loos, H., Lutman, A., Nuhn, H.-D., Ratner, D., Rzepiela, J., Shu, D., Shvyd’ko, Y., Spampinati, S., Stoupin, S., Terentyev, S., Trakhtenberg, E., Walz, D., Welch, J., Wu, J., Zholents, A. & Zhu, D. (2012). *Nat. Photon.* **6**, 693–698.

Berne, B. J. & Pecora, R. (2000). *Dynamic Light Scattering: With Applications to Chemistry, Biology and Physics*. New York: Dover.

Blaj, G., Caragiulo, P., Carini, G., Carron, S., Dragone, A., Freytag, D., Haller, G., Hart, P., Hasi, J., Herbst, R., Herrmann, S., Kenney, C., Markovic, B., Nishimura, K., Osier, S., Pines, J., Reese, B., Segal, J., Tomada, A. & Weaver, M. (2015). *J. Synchrotron Rad.* **22**, 577–583.

Bonifacio, R., Pellegrini, C. & Narducci, L. (1984). *Opt. Commun.* **50**, 373–378.

Bostedt, C., Boutet, S., Fritz, D., Huang, Z., Lee, H. J., Lemke, H. T., Robert, A., Schlotter, W. F., Turner, J. J. & Williams, G. J. (2016). *Rev. Mod. Phys.* **88**, 015007.

Carnis, J., Cha, W., Wingert, J., Kang, J., Jiang, Z., Song, S., Sikorski, M., Robert, A., Gutt, C., Chen, S.-W., Dai, Y., Ma, Y., Guo, H., Lurio, L. B., Shpyrko, O., Narayanan, S., Cui, M., Kosif, I., Emrick, T., Russell, T. P., Lee, H. C., Yu, C.-J., Grübel, G., Sinha, S. K. & Kim, H. (2014). *Sci. Rep.* **4**, 6017.

Clark, J. N., Beitra, L., Xiong, G., Higginbotham, A., Fritz, D. M., Lemke, H. T., Zhu, D., Chollet, M., Williams, G. J., Messerschmidt, M., Abbey, B., Harder, R. J., Korsunsky, A. M., Wark, J. S. & Robinson, I. K. (2013). *Science*, **341**, 56–59.

Doering, D., Chuang, Y.-D., Andresen, N., Chow, K., Contarato, D., Cummings, C., Domning, E., Joseph, J., Pepper, J. S., Smith, B.,

Zizka, G., Ford, C., Lee, W. S., Weaver, M., Patthey, L., Weizeorick, J., Hussain, Z. & Denes, P. (2011). *Rev. Sci. Instrum.* **82**, 073303.

Dragone, A., Caragiulo, P., Markovic, B., Herbst, R., Reese, B., Herrmann, S. C., Hart, P. A., Segal, J., Carini, G. A., Kenney, C. J. & Haller, G. (2014). *J. Phys. Conf. Ser.* **493**, 012012.

Emma, P., Akre, R., Arthur, J., Bionta, R., Bostedt, C., Bozek, J., Brachmann, A., Bucksbaum, P., Coffee, R., Decker, F. J., Ding, Y., Dowell, D., Edstrom, S., Fisher, A., Frisch, J., Gilevich, S., Hastings, J., Hays, G., Hering, P., Huang, Z., Iverson, R., Loos, H., Messerschmidt, M., Miahnahri, A., Moeller, S., Nuhn, H. D., Pile, G., Ratner, D., Rzepiela, J., Schultz, D., Smith, T., Stefan, P., Tompkins, H., Turner, J., Welch, J., White, W., Wu, J., Yocky, G. & Galayda, J. (2010). *Nature (London)*, **4**, 641–647.

Goodman, J. W. (2006). *Speckle Phenomena in Optics: Theory and Applications*. Englewood: Roberts.

Grübell, G., Madsen, A. & Robert, A. (2008). *Soft Matter Characterization*, edited by R. Borsali and R. Pecora, pp. 953–995. Springer Netherlands.

Gutt, C., Stadler, L.-M., Duri, A., Autenrieth, T., Leupold, O., Chushkin, Y. & Grübel, G. (2009). *Opt. Express*, **17**, 55–61.

Gutt, C., Wochner, P., Fischer, B., Conrad, H., Castro-Colin, M., Lee, S., Lehmkuhler, F., Steinke, I., Sprung, M., Roseker, W., Zhu, D., Lemke, H., Bogle, S., Fuoss, P. H., Stephenson, G. B., Cammarata, M., Fritz, D. M., Robert, A. & Grübel, G. (2012). *Phys. Rev. Lett.* **108**, 024801.

Hara, T., Inubushi, Y., Katayama, T., Sato, T., Tanaka, H., Tanaka, T., Togashi, T., Togawa, K., Tono, K., Yabashi, M. & Ishikawa, T. (2013). *Nat. Commun.* **4**, 1–5.

Hart, P., Boutet, S., Carini, G., Dragone, A., Duda, B., Freytag, D., Haller, G., Herbst, R., Herrmann, S., Kenney, C., Morse, J., Nordby, M., Pines, J., van Bakel, N., Weaver, M. & Williams, G. (2012a). *Nuclear Science Symposium and Medical Imaging Conference (NSSMIC), 2012 IEEE*, pp. 538–541.

Hart, P., Boutet, S., Carini, G., Dubrovin, M., Duda, B., Fritz, D., Haller, G., Herbst, R., Herrmann, S., Kenney, C., Kurita, N., Lemke, H., Messerschmidt, M., Nordby, M., Pines, J., Schafer, D., Swift, M., Weaver, M., Williams, G., Zhu, D., Van Bakel, N. & Morse, J. (2012b). *Proc. SPIE*, **8504**, 85040C.

Herrmann, S., Boutet, S., Duda, B., Fritz, D., Haller, G., Hart, P., Herbst, R., Kenney, C., Lemke, H., Messerschmidt, M., Pines, J., Robert, A., Sikorski, M. & Williams, G. (2013). *Nucl. Instrum. Methods Phys. Res. A*, **718**, 550–553.

Hruszkewycz, S. O., Sutton, M., Fuoss, P. H., Adams, B., Rosenkranz, S., Ludwig, K. F., Roseker, W., Fritz, D., Cammarata, M., Zhu, D., Lee, S., Lemke, H., Gutt, C., Robert, A., Grübel, G. & Stephenson, G. B. (2012). *Phys. Rev. Lett.* **109**, 185502.

Ishikawa, T., Aoyagi, H., Asaka, T., Asano, Y., Azumi, N., Bizen, T., Ego, H., Fukami, K., Fukui, T., Furukawa, Y., Goto, S., Hanaki, H., Hara, T., Hasegawa, T., Hatsui, T., Higashiya, A., Hirono, T., Hosoda, N., Ishii, M., Inagaki, T., Inubushi, Y., Itoga, T., Joti, Y., Kago, M., Kameshima, T., Kimura, H., Kirihara, Y., Kiyomichi, A., Kobayashi, T., Kondo, C., Kudo, T., Maesaka, H. M., Maréchal, X. M., Masuda, T., Matsubara, S., Matsumoto, T., Matsushita, T., Matsui, S., Nagasono, M., Nariyama, N., Ohashi, H., Ohata, T., Ohshima, T., Ono, S., Otake, Y., Saji, C., Sakurai, T., Sato, T., Sawada, K., Seike, T., Shirasawa, K., Sugimoto, T., Suzuki, S., Takahashi, S., Takebe, H., Takeshita, K., Tamasaku, K., Tanaka, H., Tanaka, R., Tanaka, T., Togashi, T., Togawa, K., Tokuhisa, A., Tomizawa, H., Tono, K., Wu, S., Yabashi, M., Yamaga, M., Yamashita, A., Yanagida, K., Zhang, C., Shintake, T., Kitamura, H. & Kumagai, N. (2012). *Nat. Photon.* **6**, 540–544.

Livet, F., Bley, F., Mainville, J., Caudron, R., Mochrie, S., Geissler, E., Dolino, G., Abernathy, D., Grübel, G. & Sutton, M. (2000). *Nucl. Instrum. Methods Phys. Res. A*, **451**, 596–609.

Lutman, A. A., Coffee, R., Ding, Y., Huang, Z., Krzywinski, J., Maxwell, T., Messerschmidt, M. & Nuhn, H.-D. (2013). *Phys. Rev. Lett.* **110**, 134801.

- Marinelli, A., Ratner, D., Lutman, A. A., Turner, J., Welch, J., Decker, F. J., Loos, H., Behrens, C., Gilevich, S., Miahnahri, A. A., Vetter, S., Maxwell, T. J., Ding, Y., Coffee, R., Wakatsuki, S. & Huang, Z. (2015). *Nat. Commun.* **6**, 6369.
- Ratner, D., Abela, R., Amann, J., Behrens, C., Bohler, D., Bouchard, G., Bostedt, C., Boyes, M., Chow, K., Cocco, D., Decker, F. J., Ding, Y., Eckman, C., Emma, P., Fairley, D., Feng, Y., Field, C., Flechsig, U., Gassner, G., Hastings, J., Heimann, P., Huang, Z., Kelez, N., Krzywinski, J., Loos, H., Lutman, A., Marinelli, A., Marcus, G., Maxwell, T., Montanez, P., Moeller, S., Morton, D., Nuhn, H. D., Rodes, N., Schlotter, W., Serkez, S., Stevens, T., Turner, J., Walz, D., Welch, J. & Wu, J. (2015). *Phys. Rev. Lett.* **114**, 054801.
- Sikorski, M., Song, S., Schropp, A., Seiboth, F., Feng, Y., Alonso-Mori, R., Chollet, M., Lemke, H. T., Sokaras, D., Weng, T.-C., Zhang, W., Robert, A. & Zhu, D. (2015). *J. Synchrotron Rad.* **22**, 599–605.
- Sorgenfrei, F., Schlotter, W. F., Beeck, T., Nagasono, M., Gieschen, S., Meyer, H., Föhlisch, A., Beye, M. & Wurth, W. (2010). *Rev. Sci. Instrum.* **81**, 043107.
- Strüder, L., Epp, S., Rolles, D., Hartmann, R., Holl, P., Lutz, G., Soltau, H., Eckart, R., Reich, C., Heinzinger, K., Thamm, C., Rudenko, A., Krasniqi, F., Kühnel, K., Bauer, C., Schröter, C., Moshhammer, R., Techert, S., Miessner, D., Porro, M., Hälker, O., Meidinger, N., Kimmel, N., Andritschke, R., Schopper, F., Weidenspointner, G., Ziegler, A., Pietschner, D., Herrmann, S., Pietsch, U., Walenta, A., Leitenberger, W., Bostedt, C., Möller, T., Rupp, D., Adolph, M., Graafsma, H., Hirsemann, H., Gärtner, K., Richter, R., Foucar, L., Shoeman, R. L., Schlichting, I. & Ullrich, J. (2010). *Nucl. Instrum. Methods Phys. Res. A*, **614**, 483–496.
- Sutton, M. (2008). *Cr Phys.* **9**, 657–667.
- White, W. E., Robert, A. & Dunne, M. (2015). *J. Synchrotron Rad.* **22**, 472–476.